

# Enhanced phase contrast transfer using ptychography combined with a pre-specimen phase plate in a scanning transmission electron microscope

Hao Yang<sup>a</sup>, Peter Ercius<sup>a</sup>, Peter D. Nellist<sup>b,c</sup>, Colin Ophus<sup>a,\*</sup>

<sup>a</sup>*Molecular Foundry, Lawrence Berkeley National Laboratory, Berkeley, CA, 94720, USA*

<sup>b</sup>*Department of Materials, University of Oxford, Parks Road, Oxford OX1 3PH, UK*

<sup>c</sup>*EPSRC SuperSTEM Facility, Daresbury Laboratory, Warrington, WA4 4AD, UK*

---

## Abstract

The ability to image light elements in both crystalline and noncrystalline materials at near atomic resolution with an enhanced contrast is highly advantageous to understand the structure and properties of a wide range of beam sensitive biological specimens and molecular hetero-structures. This requires the imaging system to have efficient phase contrast transfer at both low and high spatial frequencies. In this work we introduce a new phase contrast imaging method in a scanning transmission electron microscope (STEM) using a pre-specimen phase plate in the probe forming aperture, combined with a fast pixelated detector to record the diffraction patterns at every probe position, and phase reconstruction using Ptychography. The phase plate significantly enhances the low spatial frequency contrast transfer, and ptychography maximizes the extraction of the phase information at all spatial frequencies. In addition, the electron probe out of a Fresnel zone plate geometry remains its atomic resolution, allowing simultaneous formation of incoherent Z-contrast imaging with the ptychographic phase image. Initial experimental imaging of Au nanoparticles on a carbon support shows high contrast for both materials simultaneously. Multislice image simulations of a DNA molecule shows the capability of imaging soft matter at low dose conditions, which demonstrates the potential applications of imaging a wide range of beam sensitive materials.

**Keywords:** STEM, pixelated detectors, ptychography, phase contrast, phase plate, PCTF

---

## 1. Introduction

Imaging light elements such as biological specimens and molecular hetero-structures at atomic resolution has remained challenging due to the fact that high-energy electrons are weakly scattered by the sample, leading to only a small phase shift to the incident electron wave. For imaging such weakly scattering materials, coherent phase imaging provides higher image contrast than incoherent amplitude contrast from absorption, thermal diffuse scattering and spectroscopic signals [1]. Phase contrast imaging is generally performed in the conventional transmission electron microscope (CTEM) using deliberately injected lens aberrations. Although CTEM is widely used in low dose imaging of weakly scattering biological structures, its contrast transfer function is not efficient especially at low spatial frequencies [2]. To gain the necessary contrast, a large defocus has to be used which produces a nonlinear effect on the image contrast [3]. This effect becomes more pronounced in high resolution TEM (HRTEM) and often requires careful comparison with image simulations for a proper structure interpretation. The introduction of a post-specimen phase plate in TEM enhances the low

spatial frequency contrast transfer [4, 5], and there continues to be considerable interests in the development of such physical phase plates.

STEM is best known for its incoherent Z-contrast imaging using an annular dark field detector (ADF) and spectroscopy capabilities. However these incoherent imaging modes are unable to match the dose efficiency of coherent phase contrast imaging of weak phase objects. Coherent bright field (BF-) STEM utilises only a small portion of the coherent scattering signal and thus the efficiency of this mode is poor. An efficient phase contrast imaging mode is highly desirable. It is possible to improve the efficiency of phase contrast in STEM through detector geometry innovations, for example using an annular detector to form the annular bright field (ABF) imaging [6, 7] and a segmented detector for differential phase contrast (DPC) imaging [8, 9, 10]. Recent developments in high speed cameras enables the acquisition of two dimensional diffraction patterns at every probe position of a two dimensional electron beam raster across the specimen, forming a four dimensional STEM (4D-STEM) dataset, and the phase information can be extracted using virtual detector geometries through post-acquisition processing. For example, the atomic electric field within a thin specimen can be mapped out [11] using a “first moment” [12] DPC detector. Ptychography has also been shown

---

\*Corresponding author

Email address: cophus@gmail.com (Colin Ophus)

as an efficient phase retrieval method for 4D-STEM data [13]. It allows the formation of an efficient phase contrast under zero lens aberrations which can be simultaneously combined with Z-contrast imaging, and gives an improved phase contrast transfer compared to any fixed detector geometries including DPC and ABF [14]. Ptychography is a technique first developed by Hoppe [15] to retrieve the object phase using diffraction patterns acquired from a sequential array of overlapping illuminated areas. Ptychography has been demonstrated at both electron [16, 17] and X-ray [18, 19] wavelengths to enhance the image contrast and resolution [20]. Due to limited camera speed, a widely adopted electron ptychography approach is to use highly defocused probes that illuminate a wide region of the sample to provide a large field of view while still limiting the number of probe positions [21, 22, 23]. Such defocused probes are however incompatible with the conditions required for atomic resolution ADF imaging, and so cannot be used simultaneously with the incoherent Z-contrast imaging. A recent development using a ptychography method called Wigner-distribution deconvolution (WDD) [16, 24] and a fast pixelated detector shows that it not only allows simultaneous atomic resolution phase and ADF Z-contrast imaging, but also enables direct measurement and removal of residual lens aberrations through post-acquisition processing, and allows “optical-sectioning” to obtain three-dimensional information using only one experimental dataset under a single focusing condition [25].

Although ptychography 4D-STEM under zero defocus offers an efficient phase image that can be combined with simultaneous Z-contrast imaging, its sine-shaped contrast transfer function at low spatial frequencies [26] can still be improved. Recently, it was shown that introducing a phase plate at the probe forming aperture of a STEM is equivalent to a Zernike phase plate in the back focal plane of a TEM [27] based on the principle of reciprocity [28], and leads to a phase contrast transfer function (PCTF) that depends on the cosine of the aberration wave shift [29]. Another study demonstrated that the introduction of a patterned pre-specimen phase plate in the probe forming aperture combined with a virtual detector whose geometry matches that of the phase plate, a method called matched illumination detector interferometry (MIDI-STEM) [30], leads to a directly interpretable phase image. This approach also gives a linear contrast transfer function with enhanced low spatial frequencies. The introduction of a phase plate in X-ray diffraction experiment has also been shown to improve the phase retrieval by enhancing the interferences between the diffracted waves collected in the far field [31].

Here we introduce a 4D-STEM phase contrast imaging method, ptychographic MIDI-STEM (PMIDI-STEM), which combines the advantage of a phase plate for enhanced low spatial frequency contrast transfer demonstrated in the MIDI-STEM work [30], and the advantage of the ptychography 4D-STEM method [13, 26] to maximize the

extraction of phase information and allow simultaneous formation of incoherent Z-contrast imaging. We perform theoretical calculations to compare the PCTF of PMIDI-STEM to that of MIDI-STEM, ptychography 4D-STEM at zero defocus as well as ptychography with a largely defocused probe. We show a proof-of-principle experiment result of imaging gold nanoparticles on an ultra-thin amorphous carbon substrate, and perform multislice image simulations of a heterogeneous DNA bio-molecule attached to Au nanoparticles under low dose imaging conditions to demonstrate the potential applications of our method.

## 2. Experimental Setup

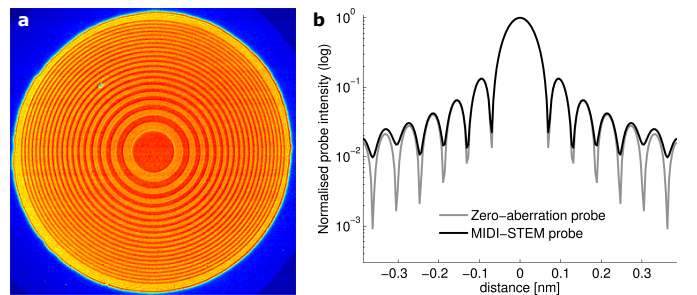


Figure 1: (a) An averaged convergent beam electron diffraction (CBED) pattern formed by scanning a MIDI-STEM electron probe with 20-ring pairs over an ultra-thin carbon sample. (b) Comparison of real space electron probe intensity (log-scale) under zero lens aberrations with and without the presence of a 20-ring pairs Fresnel type MIDI-STEM phase plate, showing that the MIDISTEM electron probe has an atomically sharp central peak with enhanced probe tails.

Fig. 1a shows an averaged convergent beam electron diffraction (CBED) pattern recorded while the electron probe with the presence of a MIDI-STEM phase plate was scanning over an ultra-thin carbon layer. The phase plate is an equal-area Fresnel zone plate with 20-ring pairs, fabricated using FIB milling of a SiN membrane [32]. With such a phase plate geometry, the electron probe remains its atomically sharp real space intensity profile 1b, which enables simultaneous incoherent Z-contrast imaging to be combined with phase imaging at atomic resolution. The MIDI-STEM probe also shows enhanced intensities at the probe tail, as compared to the intensity of the electron probe without the phase plate.

The 4D-STEM data consisting of a transmitted electron diffraction pattern at each probe position was recorded using a Gatan K2 IS direct electron detector with  $3840 \times 3712$  pixels, operated at 400 frames per second and binned by 2. The camera acquisition and probe scanning were synchronized using a Gatan Digiscan. For the experimental data demonstrated in this work, the electron probe was scanned over a 14.5nm field-of-view with  $256 \times 256$  probe positions to create a  $256 \times 256 \times 1920 \times 1792$  4D-STEM data set consisting of 420 GB of raw images.

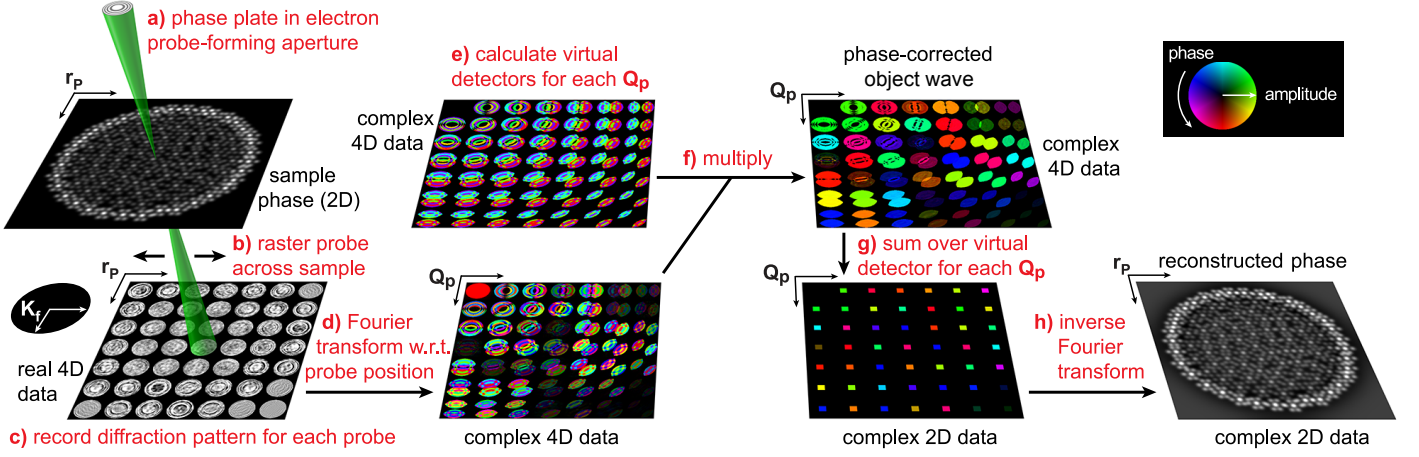


Figure 2: Schematics of the PMIDI-STEM setup and the ptychographic reconstruction procedure. (a) A phase plate is used in the probe forming aperture, and (b) a fast pixelated detector collects the diffraction patterns synchronously with the STEM probe raster-scan, forming a real 4D data cube (c). (d) The real 4D data is Fourier transformed with respect to probe positions  $\mathbf{r}_p$ , resulting in a complex 4D data in the frequency domain ( $\mathbf{Q}_p$ ) of the real space probe positions. The complex 4D data is a consequence of every diffracted electron wave interfering with its neighboring waves, and visually appear as the probe-forming apertures overlapped with a pair of apertures being shifted by  $\pm \mathbf{Q}_p$ . (e) A set of frequency ( $\mathbf{Q}_p$ ) dependent complex virtual detectors consisting of overlapping apertures can be synthesized given the geometry and the phase of the phase plate. (f) These virtual detectors can be used to remove the probe-induced phase variation inside the complex 4D data, leading to a phase-corrected object wave for each frequency  $\mathbf{Q}_p$ . (g) After phase-correction, the object function in the frequency domain ( $\mathbf{Q}_p$ ) can be calculated by integrating the complex object wave over the detector plane  $\mathbf{K}_f$ . (h) Inverse Fourier transform of the object function with respect to  $\mathbf{Q}_p$  leads to the final reconstructed complex object function in real space  $\mathbf{r}_p$ .

### 3. Theoretical background

#### 3.1. Phase retrieval with ptychography

Fig. 2 shows a schematic illustration of the ptychography reconstruction procedure used to retrieve the phase from the recorded 4D dataset. The method demonstrated here is a Fourier based direct phase retrieval method extended from the previous work [17, 13], and modified to accommodate the presence of a phase plate in the probe-forming aperture. After a 4D dataset is recorded consisting of a convergent beam electron diffraction (CBED) pattern at every probe position  $\mathbf{r}_p$ , the 4D dataset is Fourier transformed with respect to probe positions  $\mathbf{r}_p$ , which transforms the 4D data into a doubly-reciprocal space complex 4D matrix with two dimensions being the scattering vectors  $\mathbf{K}_f$  in the diffraction plane and the other two dimensions being the frequency  $\mathbf{Q}_p$  of the real space probe positions. The doubly-reciprocal space 4D matrix is named  $G(\mathbf{K}_f, \mathbf{Q}_p)$  to be consistent with the previous work [17, 13]. The Fourier transform with respect to probe positions is a key step of this ptychography method, which interferes the electron wave at every probe position with those at its neighboring positions similar to off-axis holography [33], but instead of using a physical biprism to generate a reference wave in holography, ptychography uses the diffracted electron waves at the neighboring probe positions of each electron wave as the reference.

Under the weak phase object approximation (WPOA), the doubly-reciprocal space 4D matrix  $G(\mathbf{K}_f, \mathbf{Q}_p)$  can be approximated as a linear function of the interference between the direct electron beam and two first order diffracted

beams ( $\pm \mathbf{Q}_p$ ):

$$G(\mathbf{K}_f, \mathbf{Q}_p) = |A(\mathbf{K}_f)|^2 \delta(\mathbf{Q}_p) + A(\mathbf{K}_f) A^*(\mathbf{K}_f + \mathbf{Q}_p) \Psi^*(-\mathbf{Q}_p) + A^*(\mathbf{K}_f) A(\mathbf{K}_f - \mathbf{Q}_p) \Psi(\mathbf{Q}_p), \quad (1)$$

where  $\mathbf{K}_f$  is the scattering vector and  $\mathbf{Q}_p$  is the reciprocal vector of the real space probe position  $\mathbf{r}_p$ .  $A(\mathbf{K}_f)$  is the probe forming aperture function and  $\Psi(\mathbf{Q}_p)$  is the Fourier transform of the object transmission function as a function of spatial frequency  $\mathbf{Q}_p$  and would be the scattered wave function under conditions of plane-wave illumination. Under the weak phase approximation, it has been proven [17] that the object transmission function satisfies the following:

$$\Psi(\mathbf{Q}_p) = -\Psi^*(-\mathbf{Q}_p). \quad (2)$$

Therefore, Eq. 1 can be simplified as:

$$G(\mathbf{K}_f, \mathbf{Q}_p) = |A(\mathbf{K}_f)|^2 \delta(\mathbf{Q}_p) + \Gamma_A(\mathbf{K}_f, \mathbf{Q}_p) \Psi(\mathbf{Q}_p), \quad (3)$$

where the spatial frequency  $\mathbf{Q}_p$  dependant aperture-overlap function  $\Gamma_A(\mathbf{K}_f, \mathbf{Q}_p)$  in Eq. 3 describes the interference between the first order diffracted beams and the direct electron beam, being defined as following,

$$\Gamma_A(\mathbf{K}_f, \mathbf{Q}_p) = A^*(\mathbf{K}_f) A(\mathbf{K}_f - \mathbf{Q}_p) - A(\mathbf{K}_f) A^*(\mathbf{K}_f + \mathbf{Q}_p). \quad (4)$$

Based on Eq. 3, the 4D dataset  $G(\mathbf{K}_f, \mathbf{Q}_p)$  can be expressed as a set of linear terms of  $\Gamma_A(\mathbf{K}_f, \mathbf{Q}_p) \Psi(\mathbf{Q}_p)$  for a set of experimental values of spatial frequency  $\mathbf{Q}_p$  and detector pixel  $A(\mathbf{K}_f)$ . Assuming the probe-forming aperture

function  $A(\mathbf{K}_f)$  is known, the aperture-overlap function  $\Gamma_A(\mathbf{K}_f, \mathbf{Q}_p)$  can be calculated and therefore the object transmission function  $\Psi(\mathbf{Q}_p)$  can be solved at every spatial frequency  $\mathbf{Q}_p$  from Eq. 3 directly [17, 13].

Under zero lens aberrations and no phase plate,  $A(\mathbf{K}_f)$  is a top hat function. With the presence of a MIDI-STEM phase plate [30] at the probe-forming aperture plane (see Fig. 1)  $A(\mathbf{K}_f)$  can be described as:

$$A(\mathbf{K}_f) = \begin{cases} 1, & \text{for } \mathbf{K}_f \in \text{Zone 1} \\ +i, & \text{for } \mathbf{K}_f \in \text{Zone 2}, \end{cases} \quad (5)$$

where Zone 1 and Zone 2 are regions of the phase plate with different thicknesses to produce zero (black rings) and  $\pi/2$  (white rings) phase shift, respectively. It has been shown in the previous work (supplementary information of [30]) that the geometry of the phase plate is unimportant as long as it is known. For example, the phase plate can consist of randomly distributed Zone 1 and Zone 2 regions of equal total area. In this work, we use a geometry of circular ring pairs in order to ensure an azimuthal uniform phase contrast transfer.

A schematic illustration of the modulus and phase in the aperture-overlap areas described by  $\Gamma_A(\mathbf{K}_f, \mathbf{Q}_p)$  is shown in Fig. 3. The modulus of  $\Gamma_A(\mathbf{K}_f, \mathbf{Q}_p)$  represents the strength of the phase contrast that is transferred through beam interference. As has been shown previously [13, 26], at high spatial frequencies  $\mathbf{Q}_p > \alpha$  (where  $\alpha$  is the probe convergence semi-angle), the two diffracted beams overlap with the direct beam to form two “double-overlap” regions (see Fig. 3a-c), and at low spatial frequencies  $\mathbf{Q}_p \leq \alpha$ , all three beams overlap to form a “triple-overlap” region in the center of the detector plane (see Fig. 3d-e). In the case of zero lens aberrations without a phase plate, phase information is transferred only through the double-overlap region at high and low spatial frequencies in Fig. 3a and Fig. 3b, respectively. At low spatial frequencies, the two diffracted beams with anti-phase interfere destructively under zero defocus aberration, resulting in a zero modulus in the triple-overlap region in Fig. 3d. With a largely defocused probe of 100nm, the modulus of the triple overlap region is non-zero, allowing for more phase contrast transfer through the triple-overlap region. Similar to a large defocus, when a Fresnel phase plate as described in Eq. 5 is present, the non-flat phase inside the probe forming aperture significantly alters the phase inside the double- and triple-overlap regions in Fig. 3b,c,e,f). This results in a non-zero modulus inside the triple-overlap region in Fig. 3e) and therefore an improved contrast transfer of low spatial frequency phase information through the triple-overlap region. This is due to the fact that the  $\pi/2$  phase shift by the phase plate leads to both constructive and destructive interferences between the two diffracted beams, which are anti-phase and cancel each other in the case of no phase plate and zero aberrations. At high spatial frequencies, the modulus inside the double overlap region remains the same as the case without a phase plate,

suggesting that the strength of phase contrast transfer remains unchanged at high spatial frequencies.

To maximize the extraction of phase information inside the 4D dataset and achieve the best signal to noise ratio (SNR),  $\Psi(\mathbf{Q}_p)$  is calculated at each spatial frequency  $\mathbf{Q}_p$  by making use of all of the phase information at every detector pixel  $\mathbf{K}_f$ . In the case of zero aberrations and no phase plate in the probe-forming aperture, the ptychographic reconstruction is relatively straight-forward and the object function can be reconstructed by integrating the phase (the complex quantity to be exact) inside either side of the double-overlap regions at every spatial frequency  $\mathbf{Q}_p$ , as demonstrated previously [13, 26]. The introduction of a phase plate with a  $\pi/2$  phase shift leads to phase variations inside the aperture-overlap region as shown in Fig. 3. Such phase variation can be induced by both lens aberrations and the phase plate inside probe-forming aperture, and a simple integration following the previous work [13, 26] will result in a loss of object phase information. Removing the effect of lens aberrations or the phase plate can be done by creating a complex “virtual detector” (see Fig. 2) for each spatial frequency  $\mathbf{Q}_p$  to correct the phase variation inside the complex 4D data  $G(\mathbf{K}_f, \mathbf{Q}_p)$ . The virtual detector is mathematically expressed in Eq. 6 as the normalized complex conjugate of the aperture-overlap function  $\Gamma_A(\mathbf{K}_f, \mathbf{Q}_p)$ , and to remove the phase variations inside the aperture-overlap, the complex 4D data  $G(\mathbf{K}_f, \mathbf{Q}_p)$  is simply multiplied by the virtual detector of each frequency  $\mathbf{Q}_p$ , leading to a phase-corrected object wave at every frequency  $\mathbf{Q}_p$  as shown in Fig. 2. The phase-corrected object wave is integrated over the detector plane leading to the reconstructed object function in reciprocal space following Eq. 6. Inverse Fourier transform of  $\Psi(\mathbf{Q}_p)$  with respect to the spatial frequency  $\mathbf{Q}_p$  result in the final reconstructed object function in real space.

$$\Psi(\mathbf{Q}_p) = \sum_{\mathbf{K}_f} \{G(\mathbf{K}_f, \mathbf{Q}_p) \cdot \frac{\Gamma_A^*(\mathbf{K}_f, \mathbf{Q}_p)}{|\Gamma_A(\mathbf{K}_f, \mathbf{Q}_p)|}\},$$

for  $\mathbf{K}_f \in \{|\Gamma_A(\mathbf{K}_f, \mathbf{Q}_p)| \neq 0\}$ . (6)

Note that being able to correct the probe-phase using a virtual detector in Fig. 2 allows the phase information at all detector pixels  $\mathbf{K}_f$  to be integrated to give the best phase contrast. The virtual detector also imposes an inherent filter of the noise outside the aperture-overlap region without reducing the strength of the phase signal. From a known physical geometry of the phase plate, generating virtual detectors to compensate the  $\pi/2$  phase shift from the phase plate is experimentally straightforward to implement in the ptychography algorithm. Here we simplify the issue by assuming the aperture function to have zero lens aberrations and a perfect  $\pi/2$  phase shift from the phase plate, which is reasonable for experiments running on an aberration corrected STEM and can be improved in future work using for example the ptychography Wigner-distribution deconvolution method [25] or iterative



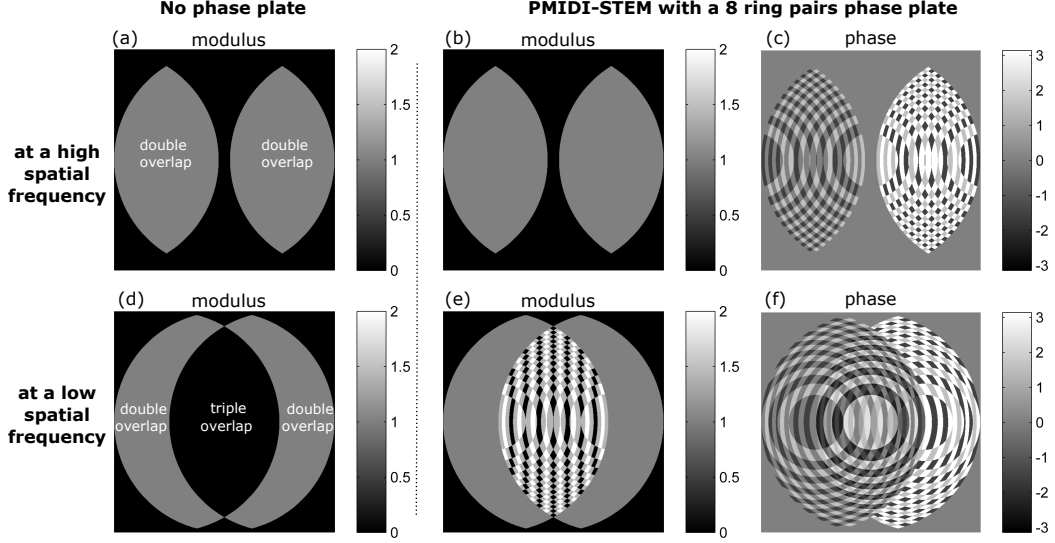


Figure 3: Schematic illustration of electron interference inside the aperture-overlap formed by two first order diffracted beams and the direct beam, as described by the function  $\Gamma_A(\mathbf{K}_f, \mathbf{Q}_p)$ . The interference between the two diffracted beams and the direct beam form two double-overlap regions at a high spatial frequency example in a,b,c), and all three beams interfere to form a triple-overlap region in the center of the detector at a low spatial frequency example in d,e,f). In the case of zero aberrations and no phase plate in a) and d),  $\Gamma_A(\mathbf{K}_f, \mathbf{Q}_p)$  has zero phase and the triple-overlap region at a low spatial frequency has zero modulus. With the presence of a phase plate in b,c,e,f),  $\Gamma_A(\mathbf{K}_f, \mathbf{Q}_p)$  shows phase variations inside the aperture-overlap and a strong modulus inside the triple-overlap region at low spatial frequencies.

ptychography methods [21]. Finally, inverse Fourier transform of  $\Psi(\mathbf{Q}_p)$  leads to the retrieved object transmission function (both modulus and phase) as a function of the real space probe position  $\psi(\mathbf{r}_p)$ .

### 3.2. PCTF calculations

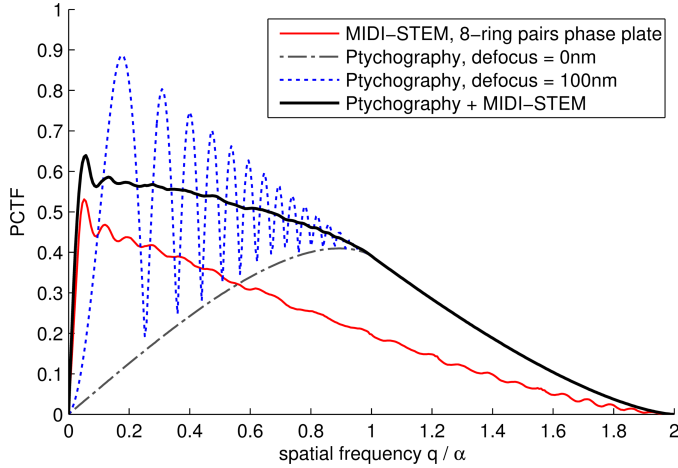


Figure 4: PCTF of Ptychography MIDI-STEM (PMIDI-STEM) with a 8-ring pairs phase plate. For comparison, the PCTF of MIDI-STEM with the same phase plate (red solid line), ptychography 4D-STEM at zero defocus (dash-dot line), as well as ptychography 4D-STEM with a 100nm defocused probe (dotted line) are shown for comparison. The maximum spatial frequency being transferred is twice the convergence semi-angle of the probe forming aperture  $\alpha$ , corresponding to a theoretical resolution limit of 0.058nm for 300keV beam energy and 17mrad convergence semi-angle.

As discussed above, Eq. 3 indicates that the phase information of the object  $\Psi(\mathbf{Q}_p)$  is transferred through

the beam interfering aperture-overlap region described by  $\Gamma_A(\mathbf{K}_f, \mathbf{Q}_p)$ . The modulus of the aperture-overlap function describes the strength of the phase information present inside the aperture-overlap regions, and thus provides a quantitative measurement of the phase being transferred. Therefore the PCTF of ptychography can be calculated as the total area of aperture-overlap regions which carry phase information (i.e., with non-zero modulus of  $\Gamma_A(\mathbf{K}_f, \mathbf{Q}_p)$ ), normalized by the the total area of the bright field disc as following:

$$\text{Ptychography: PCTF}(\mathbf{Q}_p) = \frac{1}{2} \frac{\sum_{\mathbf{K}_f} |\Gamma_A(\mathbf{K}_f, \mathbf{Q}_p)|}{\sum_{\mathbf{K}_f} |A(\mathbf{K}_f)|} \quad (7)$$

Note that under WPOA and zero aberration condition used in Eq. 2 and Eq. 3, the object phase can be determined using either  $+\mathbf{Q}_p$  or  $-\mathbf{Q}_p$  side of the overlapping discs, therefore a pre-factor of 1/2 is used in Eq. 7 for the PCTF calculations. This pre-factor in Eq. 7 leads to a PCTF value that is half of the PCTF defined in the previous work [26].

For MIDI-STEM imaging with a pixelated detector [30], the phase image is synthesized at every probe position by integrating the diffraction intensity over the virtual detector  $MIDI(\mathbf{K}_f)$  described in Eq. 8. The diffraction signal being integrated over the detector predominantly results from the dot product of the imaginary part of  $\Gamma_A(\mathbf{K}_f, \mathbf{Q}_p)$  and the phase of the object, in the same way as a HRTEM phase plate which uses a consistent  $\pi/2$  phase shift to convert the object phase to directly measurable diffraction intensities [34]. Therefore the correspond-

ing PCTF can be mathematically described as:

$$\text{MIDI}(\mathbf{K}_f) = \begin{cases} +1, & \text{for } \mathbf{K}_f \in \text{Zone 1} \\ -1, & \text{for } \mathbf{K}_f \in \text{Zone 2} \end{cases} \quad (8)$$

$$\text{MIDI: PCTF}(\mathbf{Q}_p) = \frac{\text{Im}\{\sum_{\mathbf{K}_f} (\Gamma_A(\mathbf{K}_f, \mathbf{Q}_p) \cdot \text{MIDI}(\mathbf{K}_f))\}}{2 \sum_{\mathbf{K}_f} |A(\mathbf{K}_f)|} \quad (9)$$

Fig. 4 shows the PCTF of PMIDI-STEM with 8-ring pairs, compared to that of MIDI-STEM and ptychography 4D-STEM without phase plate under both zero aberration and 100nm-defocus aberration. It can be seen that in the relatively high spatial frequency range (scattering vector  $q$  larger than the convergence angle  $\alpha$ ), ptychography gives a PCTF that is approximately twice as large as that of MIDI-STEM. In the relatively low spatial frequency range ( $q|\alpha$ ), MIDI-STEM gives a better PCTF than ptychography 4D-STEM under zero defocus condition, which has been explained qualitatively in terms of difference in the contrast transfer through the triple-overlap region shown in Fig. 3d,e). Ptychography with largely defocused probe can also enhance the contrast transfer at low frequencies, as shown in the dotted line in Fig. 4, however the PCTF varies strongly depending on the spatial frequency. In comparison, the PMIDI-STEM method demonstrated in this work by combining MIDI-STEM phase plate with ptychography gives a much smoother PCTF in the low frequency range, as compared to the largely defocused probe used by various iterative ptychography methods in literature [21, 19].

#### 4. Results and discussion

A proof of principle study was performed on a sample of Au nanoparticles on a carbon support and shown in Fig. 5. For a direct comparison, both MIDI-STEM (Fig. 5a) and PMIDI-STEM (Fig. 5b) have been applied to retrieve the phase from the same 4D data. Both images give a good contrast of both the carbon support and the Au nanoparticles because of the good sensitivity of both methods in imaging light elements. A pair of high order Fourier spots from the Au lattice is clearly visible using the PMIDI-STEM method in Fig. 5b) but not present in the MIDI-STEM image shown in Fig. 5a), suggesting that more phase information is transferred using PMIDI-STEM compared to MIDI-STEM.

In order to explore the potential limits of this new imaging method, especially in the applications of imaging beam sensitive biological structures, we performed a multislice simulation of a DNA snippet connecting two gold nanoparticles on a single layer of graphene, see Fig. 6. This is the same simulation model as used in the MIDI-STEM work [30] for a consistent comparison. Multislice image simulations were performed using custom MATLAB codes that follow the methods of Kirkland [2], using the

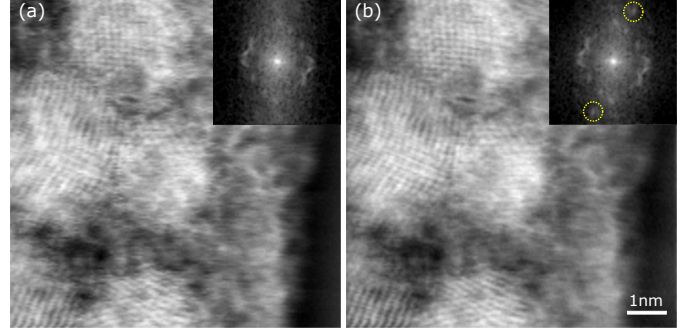


Figure 5: Experimental phase images of Au on a carbon support using (a) the MIDI-STEM method and (b) PMIDI-STEM combining ptychography with a phase plate. The experiment was performed on an aberration corrected microscope using a phase plate with 20 ring pairs. The inset shows the diffractogram of the top left part of the image consisting of 3 nanoparticles, and the dashed circles in (b) indicate diffraction spots that are visible in (b) the PMIDI-STEM phase image but not in (a) the MIDI-STEM image.

same microscope parameters as in the experiment and 8 frozen phonon configurations. Electron doses of infinity, 128, 32 and  $8e^{-}\text{\AA}^{-2}$  were used to simulate the 4D-STEM data. The noise in the simulations includes only the Poisson distributed shot noise and no detector readout noise. As seen in Fig. 6, the PMIDI-STEM method introduced in this work clearly gives the best phase image of both the DNA structure and the Au nanoparticles, as compared to MIDI-STEM and the ptychography 4D-STEM method without a phase plate. Using PMIDI-STEM, the atomic details of both the double-helix and the DNA strands are clearly visible under the dose of  $128e^{-}\text{\AA}^{-2}$ . Under an electron dose as low as  $32e^{-}\text{\AA}^{-2}$ , the signal strength remains high enough to show a higher than background image contrast in the region between two Au nanoparticles, and part of the DNA strands remain visible at this low dose. The improved low dose performance of PMIDI-STEM compared to MIDI-STEM is due to two reasons, firstly an improved PCTF over the entire spatial frequency range, and secondly the ability of ptychography to reject noise outside the disc-overlap regions which is otherwise included by the MIDI-STEM virtual detector in the final image.

Thanks to the enhanced PCTF of low spatial frequencies of PMIDI-STEM and MIDI-STEM, the visibility of the nanoparticles is improved and the shape and location of the two nanoparticles remain readily identifiable at the dose of  $8e^{-}\text{\AA}^{-2}$ , see both the phase image in Fig. 6 and the corresponding diffractogram in Fig. 7. Using the PMIDI-STEM method, the atomic fringes of the Au nanoparticles remain visible at a dose of  $8e^{-}\text{\AA}^{-2}$ . The Au lattice fringes are also visible to some extent at the dose of  $8e^{-}\text{\AA}^{-2}$  using ptychography 4D-STEM without a phase plate, but without the low spatial frequency information describing the shape and thickness profile of the nanoparticle, it's difficult to identify the location of the Au nanoparticle.

Fig. 8 shows the SNR as a function of electron dose us-

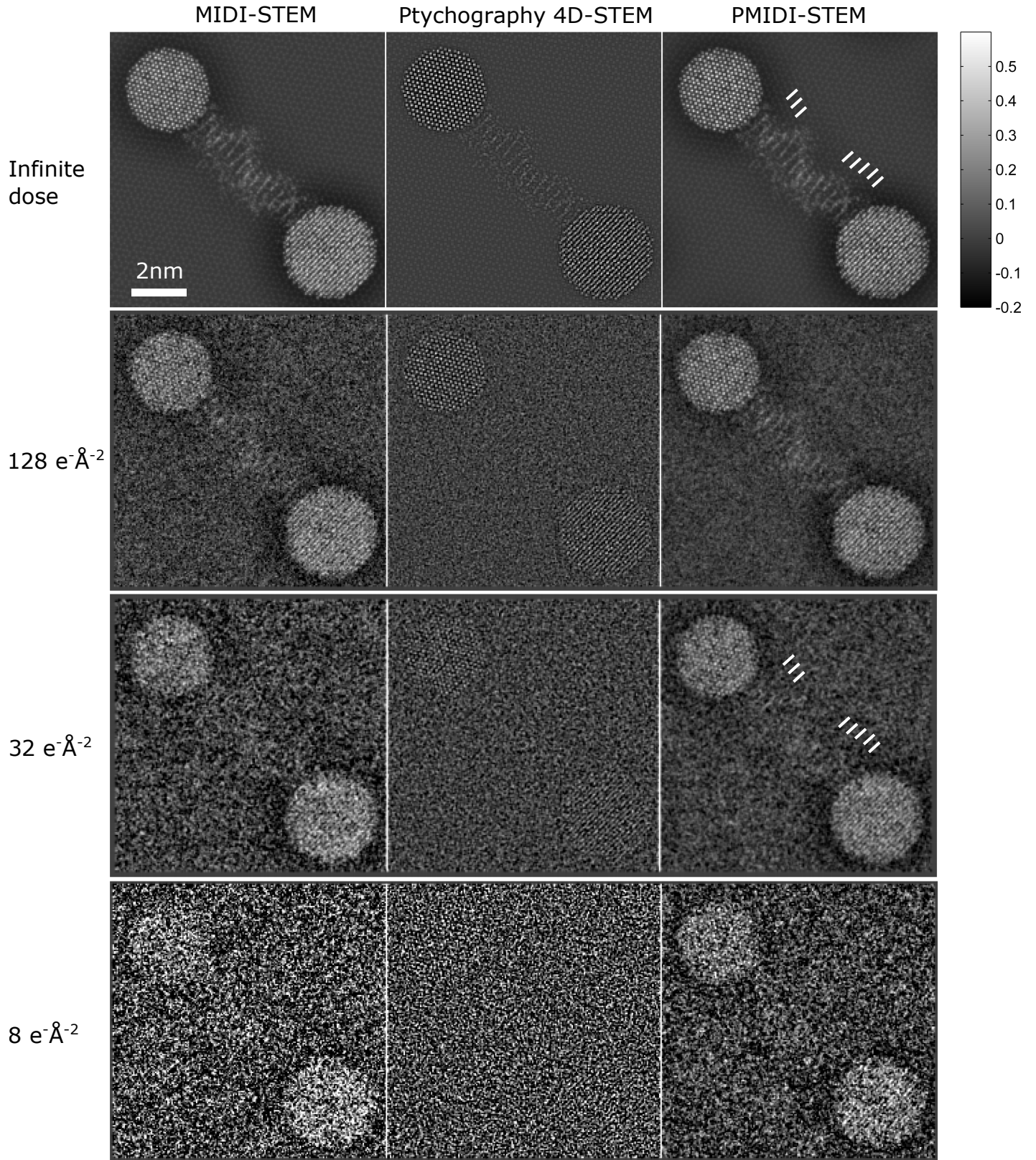


Figure 6: Multislice simulations of phase reconstruction of a DNA snippet connecting two gold nanoparticles on a single layer of graphene substrate. Phase images were reconstructed using PMIDI-STEM and MIDI-STEM virtual detector, as well as ptychography 4D-STEM without a phase plate. The images using these three methods are compared at several electron doses. The white lines indicates part of the DNA strands that are visible under the dose of  $32 \text{ e}^- \text{Å}^{-2}$ . The phases obtained from the ptychography methods are quantitative, and the scale bar is in unit of radians.



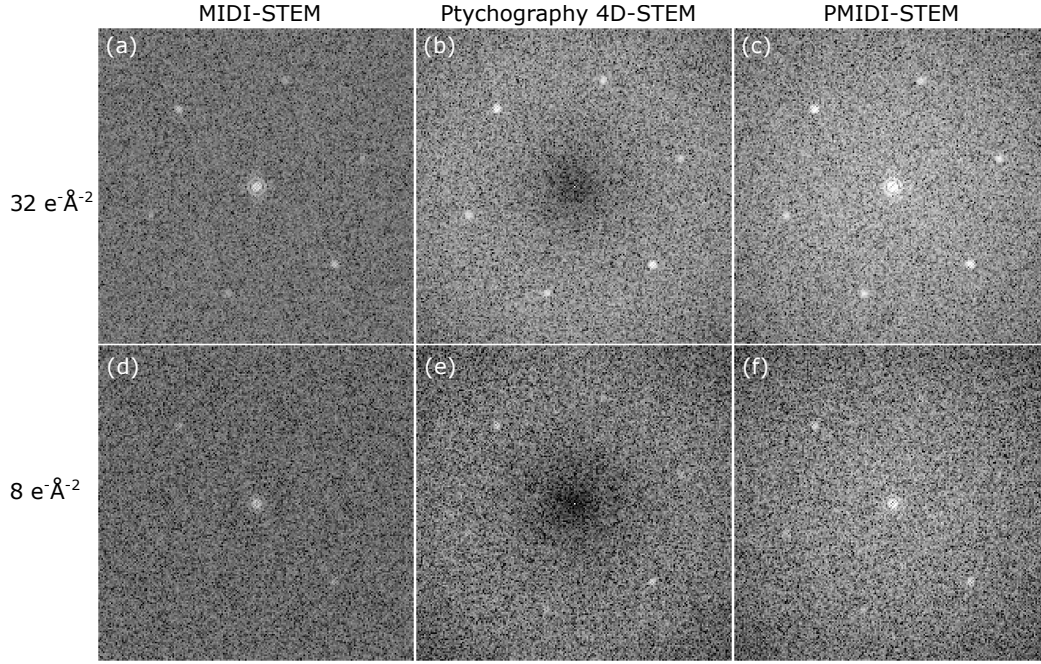


Figure 7: Diffraction patterns obtained from the Fourier transform of the phase images to compare the visibility of Au atomic lattices of different methods under the electron dose of 32 and 8  $\text{e}^- \text{\AA}^{-2}$ . The intensities of the FT images are in log scale and adjusted to have roughly the same contrast of background.

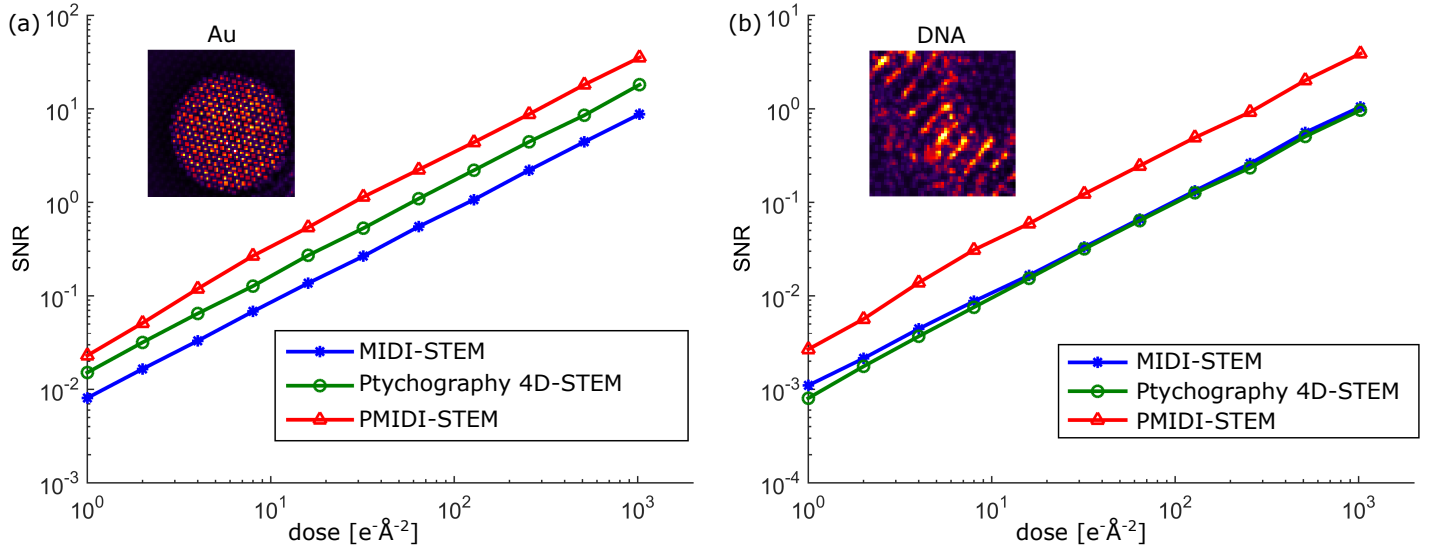


Figure 8: Comparison of phase image SNR as a function of the electron dose for the three phase retrieval methods. Two image sub-regions consisting of the Au nanoparticle and the DNA structure are used to evaluate the SNR performance of strongly-scattering and weakly-scattering objects, respectively.

ing the dose series multislice simulations of the Au/DNA structure. To evaluate the SNR of both strongly and weakly scattering objects, the SNR plots are calculated from two image regions consisting of only Au and DNA, respectively. Compared to the MIDI-STEM method, the PMIDI-STEM method combining ptychography with the MIDI-STEM phase plate shows more than a factor of two improvement in SNR for imaging both Au lattice and DNA. And the SNR of ptychography 4D-STEM is better than that of MIDI-STEM for imaging Au atomic lattices, which is consistent with the PCTF plot showing a better high frequency contrast transfer using ptychography 4D-STEM than using MIDI-STEM.

## 5. Conclusion

In this work we demonstrated a new STEM phase imaging method which combines a phase plate in the probe-forming aperture, a fast pixelated detector to record the 4D-STEM data, and a ptychography phase reconstruction method. Theoretical calculations suggest this method gives a close to linear PCTF that is efficient in both low and high spatial frequencies. A proof of principle experiment demonstrates the sensitivity of this imaging method for both light and heavy elements, and the improved PCTF leads to more information transfer compared to MIDI-STEM. Low dose multislice image simulations on a Au-DNA snippet sample suggests that it's promising to image soft matter at nearly atomic resolution with a close to "critical dose" of less than  $50\text{e}^- \text{\AA}^{-2}$ . The low dose performance of this technique provides an opportunity to image a wide range of beam sensitive materials and biological structures. The sensitivity to both light and heavy elements at both low and high spatial frequencies is particularly interesting in imaging hetero-structures composed of both hard and soft matter especially at their interface. The linear PCTF offers a directly interpretable phase image without comparing to image simulations, and the phase image can be obtained at zero defocus, which is highly advantageous compared to the large defocus values required for phase contrast imaging in CTEM. The fact that the STEM probe remains its atomic resolution with the presence of the phase plate allows simultaneous atomic resolution incoherent ADF imaging to be combined with the phase image, which can be very beneficial compared to ptychography methods using largely defocused probe.

## Acknowledgements

Work at the Molecular Foundry was supported by the Office of Science, Office of Basic Energy Sciences, of the U.S. Department of Energy under Contract No. DE-AC02-05CH11231. The phase plates used in the experimental portion of this study were fabricated and tested by Jordan Pierce, Tyler Harvey, Jordan Chess and Ben McMorran.

## References

- [1] R. Henderson, The potential and limitations of neutrons, electrons and x-rays for atomic resolution microscopy of unstained biological molecules, *Quart. Rev. Biophys.* 28 (02) (1995) 171–193.
- [2] E. Kirkland, *Advanced computing in electron microscopy*, Springer Science & Business Media, 2010.
- [3] K. Downing, R. Glaeser, Restoration of weak phase-contrast images recorded with a high degree of defocus: the twin image problem associated with ctf correction, *Ultramicroscopy* 108 (9) (2008) 921–928.
- [4] R. Danev, B. Buijsse, M. Khoshouei, J. Plitzko, W. Baumeister, Volta potential phase plate for in-focus phase contrast transmission electron microscopy, *Proceedings of the National Academy of Sciences* 111 (44) (2014) 15635–15640.
- [5] E. Majorovits, B. Barton, K. Schultheiss, F. Perez-Willard, D. Gerthsen, R. Schröder, Optimizing phase contrast in transmission electron microscopy with an electrostatic (boersch) phase plate, *Ultramicroscopy* 107 (2) (2007) 213–226.
- [6] H. Rose, Phase contrast in scanning transmission electron microscopy, *Optik* 39 (4) (1974) 416–436.
- [7] S. Findlay, N. Shibata, H. Sawada, E. Okunishi, Y. Kondo, Y. Ikuhara, Dynamics of annular bright field imaging in scanning transmission electron microscopy, *Ultramicroscopy* 110 (7) (2010) 903–923.
- [8] N. Dekkers, H. De Lang, Differential phase contrast in a stem, *Optik* 41 (4) (1974) 452–456.
- [9] H. Rose, Nonstandard imaging methods in electron microscopy, *Ultramicroscopy* 2 (1977) 251–267.
- [10] N. Shibata, S. Findlay, Y. Kohno, H. Sawada, Y. Kondo, Y. Ikuhara, Differential phase-contrast microscopy at atomic resolution, *Nature Physics* 8 (8) (2012) 611–615.
- [11] K. Müller, F. Krause, A. Béché, M. Schowalter, V. Galioit, S. Löffler, J. Verbeeck, J. Zweck, P. Schattschneider, A. Rosebauer, Atomic electric fields revealed by a quantum mechanical approach to electron picodiffraction, *Nature communications* 5.
- [12] E. Waddell, J. Chapman, Linear imaging of strong phase objects using asymmetrical detectors in stem, *Optik* 54 (2) (1979) 83–96.
- [13] T. Pennycook, A. Lupini, H. Yang, M. Murfitt, L. Jones, P. Nellist, Efficient phase contrast imaging in stem using a pixelated detector. part 1: Experimental demonstration at atomic resolution, *Ultramicroscopy* 151 (2015) 160–167.
- [14] H. Yang, L. Jones, H. Ryll, M. Simson, H. Soltau, Y. Kondo, R. Sagawa, H. Banba, I. MacLaren, P. Nellist, 4d stem: High efficiency phase contrast imaging using a fast pixelated detector, in: *Journal of Physics: Conference Series*, Vol. 644, IOP Publishing, 2015, p. 012032.
- [15] W. Hoppe, Beugung im inhomogenen primärstrahlwellenfeld. i. prinzip einer phasenmessung von elektronenbeugungsinterferenzen, *Acta Crystallographica Section A: Crystal Physics, Diffraction, Theoretical and General Crystallography* 25 (4) (1969) 495–501.
- [16] J. Rodenburg, R. Bates, The theory of super-resolution electron microscopy via wigner-distribution deconvolution, *Philosophical Transactions of the Royal Society of London A: Mathematical, Physical and Engineering Sciences* 339 (1655) (1992) 521–553.
- [17] J. Rodenburg, B. McCallum, P. Nellist, Experimental tests on double-resolution coherent imaging via stem, *Ultramicroscopy* 48 (3) (1993) 304–314.
- [18] J. Rodenburg, A. Hurst, A. Cullis, B. Dobson, F. Pfeiffer, O. Bunk, C. David, K. Jefimovs, I. Johnson, Hard-x-ray lensless imaging of extended objects, *Physical review letters* 98 (3) (2007) 034801.
- [19] P. Thibault, M. Dierolf, A. Menzel, O. Bunk, C. David, F. Pfeiffer, High-resolution scanning x-ray diffraction microscopy, *Science* 321 (5887) (2008) 379–382.
- [20] P. Nellist, B. McCallum, J. Rodenburg, Resolution beyond the 'information limit' in transmission electron microscopy, *Nature* 374 (6523) (1995) 630–632.



- [21] A. Maiden, J. Rodenburg, An improved ptychographical phase retrieval algorithm for diffractive imaging, *Ultramicroscopy* 109 (10) (2009) 1256–1262.
- [22] M. Humphry, B. Kraus, A. Hurst, A. Maiden, J. Rodenburg, Ptychographic electron microscopy using high-angle dark-field scattering for sub-nanometre resolution imaging, *Nat. Commun.* 3 (2012) 730.
- [23] A. D’Alfonso, A. Morgan, A. Yan, P. Wang, H. Sawada, A. Kirkland, L. Allen, Deterministic electron ptychography at atomic resolution, *Physical Review B* 89 (6) (2014) 064101.
- [24] H. N. Chapman, Phase-retrieval x-ray microscopy by wigner-distribution deconvolution, *Ultramicroscopy* 66 (3) (1996) 153–172.
- [25] H. Yang, R. Rutte, L. Jones, M. Simson, R. Sagawa, H. Ryll, M. Huth, H. Pennycook, TJ Soltau, Y. Kondo, B. Davis, Image phase measurement using ptychography in the scanning transmission electron microscope, submitted.
- [26] H. Yang, T. Pennycook, P. Nellist, Efficient phase contrast imaging in stem using a pixelated detector. part ii: Optimisation of imaging conditions, *Ultramicrosc.* 151 (2015) 232–239.
- [27] R. Danev, H. Okawara, N. Usuda, K. Kametani, K. Nagayama, A novel phase-contrast transmission electron microscopy producing high-contrast topographic images of weak objects, *Journal of biological physics* 28 (4) (2002) 627–635.
- [28] J. Cowley, Image contrast in a transmission scanning electron microscope, *Applied Physics Letters* 15 (2) (1969) 58–59.
- [29] H. Minoda, T. Tamai, H. Iijima, F. Hosokawa, Y. Kondo, Phase-contrast scanning transmission electron microscopy, *Microscopy* (2015) dfv011.
- [30] C. Ophus, J. Ciston, J. Pierce, T. R. Harvey, J. Chess, B. J. McMorran, C. Czarnik, H. H. Rose, P. Ercius, Efficient linear phase contrast in scanning transmission electron microscopy with matched illumination and detector interferometry, *Nature communications* 7.
- [31] I. Johnson, K. Jefimovs, O. Bunk, C. David, M. Dierolf, J. Gray, D. Renker, F. Pfeiffer, Coherent diffractive imaging using phase front modifications, *Physical review letters* 100 (15) (2008) 155503.
- [32] T. R. Harvey, J. S. Pierce, A. K. Agrawal, P. Ercius, M. Linck, B. J. McMorran, Efficient diffractive phase optics for electrons, *New J. Phys.* 16 (9) (2014) 093039.
- [33] H. Lichte, Electron image plane off-axis holography of atomic structures, *Advances in optical and electron microscopy* 12 (1991) 25–91.
- [34] R. Danev, K. Nagayama, Complex observation in electron microscopy: Iv. reconstruction of complex object wave from conventional and half plane phase plate image pair, *Journal of the Physical Society of Japan* 73 (10) (2004) 2718–2724.